
REVISITING PSF MODELS: UNIFYING FRAMEWORK AND HIGH-PERFORMANCE IMPLEMENTATION

A PREPRINT

Yan Liu¹

Vasiliki Stergiopoulou^{2,3}

Jonathan Chuah¹

Michael Unser¹

Daniel Sage¹

Jonathan Dong^{1*}

¹Biomedical Imaging Group, École Polytechnique Fédérale de Lausanne, Lausanne, Switzerland

²LCAV, École Polytechnique Fédérale de Lausanne, Lausanne, Switzerland

³GALATEA, École Polytechnique Fédérale de Lausanne, Lausanne, Switzerland

February 6, 2025

ABSTRACT

Localization microscopy often relies on detailed models of point spread functions. For applications such as deconvolution or PSF engineering, accurate models for light propagation in imaging systems with high numerical aperture are required. Different models have been proposed based on 2D Fourier transforms or 1D Bessel integrals. The most precise ones combine a vectorial description of the electric field and precise aberration models. However, it may be unclear which model to choose, as there is no comprehensive comparison between the Fourier and Bessel approaches yet. Moreover, many existing libraries are written in Java (e.g. our previous PSF generator software) or MATLAB, which hinders the integration into deep learning algorithms. In this work, we start from the original Richards-Wolf integral and revisit both approaches in a systematic way. We present a unifying framework in which we prove the equivalence between the Fourier and Bessel strategies and detail a variety of correction factors applicable to both of them. Then, we provide a high-performance implementation of our theoretical framework in the form of an open-source library that is built on top of PyTorch, a popular library for deep learning. It enables us to benchmark the accuracy and computational speed of different models, thus allowing for an in-depth comparison of the existing models for the first time. We show that the Bessel strategy is optimal for axisymmetric beams while the Fourier approach can be applied to more general scenarios. Our work enables efficient PSF computation on CPU or GPU, which can then be included in simulation and optimization pipelines.

Keywords point spread function · localization microscopy · vectorial field propagation · open-source library

1 Introduction

The point spread function (PSF), also referred to as the impulse response, is a fundamental concept that encapsulates the key features of an optical microscope. Its monitoring and assessment have been long-standing routines in microscopy, supported by the development of specific tools [1, 2, 3] and the creation of a consortium to standardize best practices [4]. Detailed characterization of the PSF is essential to design computational imaging processes, such as single-molecule localization microscopy [5] and super-resolution microscopy, including 3D deconvolution microscopy [6, 7], structured illumination microscopy (SR-SIM) [8, 9], fluctuation microscopy [10, 11], stimulated emission-depletion microscopy (STED) [12], and MINFLUX [13]. The PSF is at the heart of these localization techniques to achieve a spatial resolution beyond the optical diffraction limit.

*Email: jonathan.dong@epfl.ch

The PSF can be measured experimentally from a z-stack of tiny fluorescent beads [6, 14]. However, a theoretical PSF is often required. Here, the challenge lies in the accurate model of light propagation for imaging systems with high numerical aperture (NA). Detailed models have been proposed [15, 16, 17, 18] to (a) go beyond simple paraxial approximations, (b) take into account the vectorial nature of the electric field, and (c) include various aberration factors, such as Gibson-Lanni aberrations due to refraction at different planar interfaces [19]. Several software packages have been developed to generate precise theoretical 3D PSFs that include various features and different aberrations. Among these, the Huygens PSF software² is well-known in the microscopy community, and our Java-based ImageJ/FIJI plugin, PSF Generator [20], has also been widely used, though it is now outdated in terms of implementation and software design. Other open-source alternatives include MATLAB-based solutions [21, 3, 22] as well as Python-based tools [23, 24].

These computational PSF models have been applied in various applications in fluorescence microscopy. For example, fitting a theoretical PSF to a measured one can improve accuracy [20, 25]. Detailed models enable quantification of 3D uncertainty [26] and PSF engineering takes full advantage of parametric PSF models [27, 28, 29]. They are a key component to create for example high-quality SMLM images [30, 31], including single-particle tracking [32, 33], and virtual SMLM microscopes [34, 35].

Existing approaches to compute the PSF can be categorized into two classes: those based on 2D Fourier transforms [16, 3] or 1D integrals of Bessel functions [15, 36, 17, 18]. These two classes of models have different assumptions (Bessel models being more restrictive) and bring different computational trade-offs. Most of these works focus on one of the two approaches, and the relationship between them remains unclear. For instance, the Gibson-Lanni aberrations [19] or the apodization factor [15] are only applied to the Bessel case, even though they could be generalized to both. To the best of our knowledge, there has not been a systematic benchmark of the two strategies yet in terms of accuracy and computational speed.

In this work, we propose a unifying framework for PSF models, in which we show the equivalence between the Fourier and Bessel approaches as different parametrizations of the same propagation integral. This enables us to generalize diverse correction factors and apply them to both models. Eventually, the choice is simplified to scalar versus vectorial models, optionally with additional correction factors. We then distribute an open-source PyTorch-based library, called `psf-generator`, which inherits all the functionalities of PyTorch and allows for a seamless integration with modern learning-based algorithms. We benchmark the two classes of models on CPU and GPU and show that the Bessel model is advantageous for axisymmetric PSFs while the Fourier one is more general, and thus more suitable for applications such as PSF engineering. Our benchmark can be updated regularly to follow the latest hardware and software developments.

2 Background

Electromagnetic waves in optical systems are fundamentally described by the Helmholtz wave equations yet solving these equations in full generality is computationally intractable. Various approximations and integral formulations have thus been developed. The cornerstone for precise PSF models in high-NA systems is the Richards-Wolf integral [15], which can be viewed as a vectorial extension of the Debye integral [37]. The conditions of validity for the Richards-Wolf integral have been thoroughly discussed by [38]. While alternative light propagation models exist, the Huygens-Fresnel approach has been shown to be equivalent, to some extent, for PSF calculations [39].

This has been the basis of a line of work for PSF models based on Bessel functions, which we will later refer to as the spherical parametrization of the Richards-Wolf integral. This approach includes simpler formulations like the Kirchhoff model and more sophisticated vectorial representations [17, 18]. These models have progressively been refined by incorporating various correction factors to account for additional physical processes: the Gibson-Lanni model for spherical aberrations due to refractive index mismatch [19] (later generalized in [40, 36]), apodization factors for energy conservation [15], and Fresnel transmission coefficients for accurate interface modeling [17]. Models using this spherical parametrization have been implemented in various software libraries in Java [20] and Python [23], which makes it widely accessible to researchers, albeit with some limitations in computational efficiency and integration with deep-learning frameworks.

Another line of work on PSF modeling is based on Fourier transforms, both in scalar [41] and vectorial [16] formulations. These models are based on a Cartesian parametrization of the underlying Richards-Wolf integral and they represent a more general counterpart of the spherical parametrization. Recently, these high-NA Fourier models have been implemented in MATLAB [3] and Tensorflow as part of a PSF fitting library [42]. Adequate sampling of the Fourier

²<https://svi.nl/>

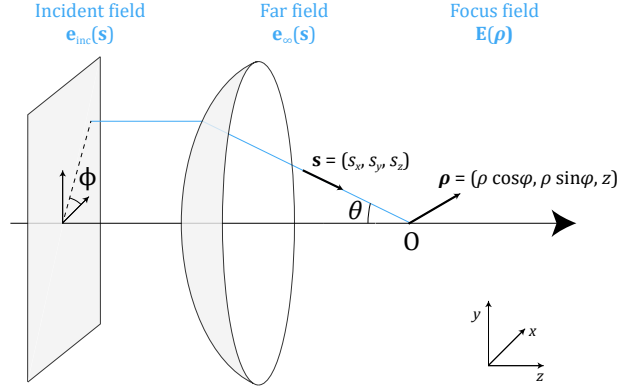


Figure 1: Geometry of the focusing of optical fields. An incident field \mathbf{e}_{inc} is transformed by a focusing element into a converging spherical wave \mathbf{e}_{∞} . These fields are parametrized by a unit vector \mathbf{s} , either in Cartesian coordinates (s_x, s_y, s_z) or spherical coordinates (θ, ϕ) . The focus field \mathbf{E} is parametrized by $\boldsymbol{\rho} = (x, y, z)$, rewritten here to introduce cylindrical coordinates ρ and ϕ .

transform is crucial for obtaining high-resolution PSFs and avoiding aliasing. A common trick based on the chirp Z transform is usually implemented to achieve it [16, 3, 29].

3 Theory

3.1 The Richards-Wolf Model

As depicted in Fig. 1, the PSF is obtained by computing the propagation of light after going through a focusing element, typically a microscope objective or lens. The incident field $\mathbf{e}_{\text{inc}}(\mathbf{s})$, also called pupil function, is represented by a disk with a maximal cut-off angle defined by the NA of the imaging system. The focusing element transforms the incident field into a spherical wave, $\mathbf{e}_{\infty}(\mathbf{s})$, evaluated on the Gaussian reference sphere. This corresponds to an ensemble of far fields propagating with direction \mathbf{s} all converging to the focal point O . Our goal is to compute the focused electric field $\mathbf{E}(\boldsymbol{\rho})$ around the point O . Thanks to the reciprocity of light propagation, this model can also be extended to the emission of a point source to the back focal plane of a microscope objective but this is not the focus of the current study.

The model introduced by [15] is the starting point that allows us to derive all the precise PSF models described in previous works. The focal field is given by a sum of plane waves with direction $\mathbf{s} = (s_x, s_y, s_z)$:

$$\mathbf{E}(\boldsymbol{\rho}) = -\frac{ifk}{2\pi} \iint_{\Omega} \mathbf{e}_{\infty}(\mathbf{s}) \exp\{ik\mathbf{s} \cdot \boldsymbol{\rho}\} d\Omega \quad (1)$$

where $\boldsymbol{\rho} = (x, y, z) = (\rho \cos \phi, \rho \sin \phi, z)$ is the position vector in the focal region of the lens, $\mathbf{s} = (s_x, s_y, s_z) = (\sin \theta \cos \phi, \sin \theta \sin \phi, \cos \theta)$ is a unit vector describing the direction of an incoming ray, f is the focal length of the lens, $k = \frac{2\pi n}{\lambda}$ is the wavenumber, λ is the wavelength, n is the refractive index of the propagation medium, and $\mathbf{e}_{\infty}(\mathbf{s})$ describes the field distribution on the Gaussian reference sphere. We integrate over set Ω of solid angles defined on a region $s_x^2 + s_y^2 \leq s_{\text{max}}^2$, where $s_{\text{max}} = \frac{\text{NA}}{n_i}$ is the cut-off determined by the NA. The angle θ is defined in the immersion medium. Correction factors are typically introduced in this expression but we will first describe the different classes of models based on this simplified concise equation.

3.2 Scalar Models

As a first step, it is common to employ a scalar approximation to simplify calculations, especially in low-NA scenarios. In this case, the far field is equal to the incident field, i.e. $e_{\infty}(\mathbf{s}) = e_{\text{inc}}(\mathbf{s})$ and the focal field is given by:

$$E(\boldsymbol{\rho}) = -\frac{ifk}{2\pi} \iint_{\Omega} e_{\infty}(s_x, s_y) \exp\{ik\mathbf{s} \cdot \boldsymbol{\rho}\} d\Omega. \quad (2)$$

This expression involves a two-dimensional integral over the pupil disk. Two possible parametrizations that yield the two classes of models described previously can be employed.

The Cartesian parametrization utilizes both s_x and s_y coordinates with $d\Omega = ds_x ds_y / s_z$, resulting in:

$$E(\boldsymbol{\rho}) = -\frac{ifk}{2\pi} \iint_{s_x^2 + s_y^2 \leq s_{\max}^2} \frac{e_{\infty}(s_x, s_y)}{s_z} \exp\{ik s_z z\} \exp\{ik(s_x x + s_y y)\} ds_x ds_y. \quad (3)$$

In this form, the focused field at a given transverse plane is given by the 2D inverse Fourier transform of $(e_{\infty}(s_x, s_y) \exp\{ik s_z z\} / s_z)$, where $s_z = \sqrt{1 - s_x^2 - s_y^2}$. Thus, the Cartesian parametrization of the Richards-Wolf integral leverages the speed and efficiency of the Fast Fourier Transform (FFT) algorithm.

Alternatively, the spherical approach parametrizes the problem with two angles $\theta \in [0, \theta_{\max}]$ (the maximum angle θ_{\max} is determined by the NA) and $\phi \in [0, 2\pi]$, as depicted in Figure 1. With $\boldsymbol{\rho} = (x, y, z) = (\rho \cos \varphi, \rho \sin \varphi, z)$ and $d\Omega = \sin \theta d\theta d\phi$, the field in the focal region can be rewritten as:

$$E(\boldsymbol{\rho}) = -\frac{ifk}{2\pi} \int_0^{\theta_{\max}} d\theta \int_0^{2\pi} d\phi e_{\infty}(\theta, \phi) \exp\{ik\rho \sin \theta \cos(\phi - \varphi)\} \exp\{ikz \cos \theta\} \sin \theta. \quad (4)$$

Eq. (4) can be further simplified if one assumes that the pupil function is axisymmetric (rotational invariant), i.e. $e_{\infty}(\theta, \phi) = e_{\infty}(\theta)$. In this case the integral over ϕ in Eq. (4) can be computed explicitly using the Bessel function J_0 ³:

$$E(\boldsymbol{\rho}) = -ifk \int_0^{\theta_{\max}} d\theta e_{\infty}(\theta) J_0(k\rho \sin \theta) \exp\{ikz \cos \theta\} \sin \theta. \quad (5)$$

Defocus is included in these models using the defocus phase factor $\exp\{ik s_z z\} = \exp\{ikz \cos \theta\}$ where z is the defocus distance. This expression, also known as angular spectrum propagation [41], accurately models the propagation of electric field in a homogeneous medium.

3.3 Vectorial Models

As the electric field is a vectorial quantity, vectorial propagation models are necessary to accurately account for the propagation and crosstalk between the different components of the vector field. Employing these precise vectorial models is crucial for high-NA systems in which case the need to consider high angles arises.

In the vectorial model, the far field $\mathbf{e}_{\infty}(\mathbf{s})$ now has a more complex dependence on the incident field $\mathbf{e}_{\text{inc}}(\mathbf{s})$ as we need to perform the basis change from a cylindrical to a spherical coordinate system:

$$\mathbf{e}_{\infty}(\theta, \phi) = \begin{bmatrix} q_s(1 - \cos 2\phi) + q_p(1 + \cos 2\phi) \cos \theta \\ (-q_s + q_p \cos \theta) \sin 2\phi \\ -2q_p \cos \phi \sin \theta \end{bmatrix} \frac{e_{\text{inc}}^x(\theta, \phi)}{2} + \begin{bmatrix} (-q_s + q_p \cos \theta) \sin 2\phi \\ q_s(1 + \cos 2\phi) + q_p(1 - \cos 2\phi) \cos \theta \\ -2q_p \sin \phi \sin \theta \end{bmatrix} \frac{e_{\text{inc}}^y(\theta, \phi)}{2} \quad (6)$$

where $\mathbf{e}_{\text{inc}} = [e_{\text{inc}}^x, e_{\text{inc}}^y, 0]$. Fresnel transmission coefficients q_s and q_p have been introduced to account for partial reflection at interfaces, which depend on the polarization state and incidence angle. For each of the s and p polarizations, they correspond to the product of all transmission coefficients for each interface from medium j to $j + 1$:

$$q_s^j = \frac{2n_j \cos \theta_j}{n_j \cos \theta_j + n_{j+1} \cos \theta_{j+1}}, \quad (7)$$

$$q_p^j = \frac{2n_j \cos \theta_j}{n_{j+1} \cos \theta_j + n_j \cos \theta_{j+1}}. \quad (8)$$

³The spherical parametrization often uses the following identities where J_n is the Bessel function of n th-order of the first kind:

$$\int_0^{2\pi} \cos(n\phi) \exp\{ix \cos(\phi - \varphi)\} d\phi = 2\pi(i)^n J_n(x) \cos(n\varphi)$$

$$\int_0^{2\pi} \sin(n\phi) \exp\{ix \cos(\phi - \varphi)\} d\phi = 2\pi(i)^n J_n(x) \sin(n\varphi)$$

The Cartesian parametrization of the vectorial model consists of the following integral:

$$\mathbf{E}(\boldsymbol{\rho}) = -\frac{ifk}{2\pi} \iint_{s_x^2 + s_y^2 \leq s_{\max}^2} \frac{\mathbf{e}_{\infty}(s_x, s_y)}{s_z} \exp\{ik s_z z\} \exp\{ik(s_x x + s_y y)\} ds_x ds_y, \quad (9)$$

which essentially boils down to computing the inverse Fourier Transform of $(\mathbf{e}_{\infty}(s_x, s_y) \exp\{ik s_z z\}/s_z)$, similar to the scalar case.

Using coordinate transformations similar to the scalar case, we can derive the spherical parametrization of the field in the focal region:

$$\mathbf{E}(\boldsymbol{\rho}) = -\frac{ifk}{2\pi} \int_0^{\theta_{\max}} d\theta \int_0^{2\pi} d\phi \mathbf{e}_{\infty}(\theta, \phi) \exp\{ik\rho \sin\theta \cos(\phi - \varphi)\} \exp\{ikz \cos\theta\} \sin\theta. \quad (10)$$

Inserting (6) into (10) and using the axisymmetric assumption of the incident field, we can obtain a simplified expression for the focal field as follows:

$$\mathbf{E}(\boldsymbol{\rho}) = -\frac{ifk}{2} \begin{bmatrix} [I_0^x - I_2^x \cos 2\varphi] - I_2^y \sin 2\varphi \\ -I_2^x \sin 2\varphi + [I_0^y + I_2^y \cos 2\varphi] \\ -2iI_1^x \cos \varphi - 2iI_1^y \sin \varphi \end{bmatrix} \quad (11)$$

where

$$I_0^a(\rho, z) = \int_0^{\theta_{\max}} e_{\text{inc}}^a(\theta) \sin\theta (\cos\theta + 1) J_0(k\rho \sin\theta) \exp\{ikz \cos\theta\} d\theta \quad (12)$$

$$I_1^a(\rho, z) = \int_0^{\theta_{\max}} e_{\text{inc}}^a(\theta) \sin^2\theta J_1(k\rho \sin\theta) \exp\{ikz \cos\theta\} d\theta \quad (13)$$

$$I_2^a(\rho, z) = \int_0^{\theta_{\max}} e_{\text{inc}}^a(\theta) \sin\theta (\cos\theta - 1) J_2(k\rho \sin\theta) \exp\{ikz \cos\theta\} d\theta \quad (14)$$

with $a \in \{x, y\}$ and $\mathbf{e}_{\text{inc}}(\theta) = [e_{\text{inc}}^x(\theta), e_{\text{inc}}^y(\theta), 0]$.

3.4 Correction Factors

Precise PSF models commonly include several physical effects which may affect the PSF. They are added as amplitude factors $a(\mathbf{s})$ and phase factors $W(\mathbf{s})$ in the original integral over solid angles in Eq. 1:

$$\mathbf{E}(\boldsymbol{\rho}) = -\frac{ifk}{2\pi} \iint_{\Omega} a(\mathbf{s}) \exp\{iW(\mathbf{s})\} \mathbf{e}_{\infty}(\mathbf{s}) \exp\{ik\mathbf{s} \cdot \boldsymbol{\rho}\} d\Omega. \quad (15)$$

Eq. (15) enables us to express these correction factors with full generality: in both vectorial and scalar models, for both Cartesian and spherical parametrizations. We present a detailed list of these correction factors in Section 3.4.1-3.4.4 and a graphical description of them in Figure 2.

3.4.1 Aberrations Due to Refractive Index Mismatch

Microscopes typically have stratified layers of different refractive indices. The biological sample is usually aqueous, on top of which we place a coverslip made of glass, and the whole sample is then put in a water or oil immersion medium to increase the numerical aperture. The microscope objectives are designed to provide aberration-free images in a specific setting with design values for refractive indices and thicknesses of the different layers. Any mismatch introduces spherical aberrations due to refraction at the different layers. These aberrations can be computed using the following formula⁴:

$$W(\mathbf{s}) = \frac{2\pi}{\lambda} \left(t_s \sqrt{n_s^2 - n_i^2 \sin^2 \theta} + t_i \sqrt{n_i^2 - n_i^2 \sin^2 \theta} - t_i^* \sqrt{n_i^{*2} - n_i^2 \sin^2 \theta} + t_g \sqrt{n_g^2 - n_i^2 \sin^2 \theta} - t_g^* \sqrt{n_g^{*2} - n_i^2 \sin^2 \theta} \right) \quad (16)$$

⁴Correction factors will be expressed in spherical coordinates. $\sin\theta$ is computed in the Cartesian case using $\sin\theta = \frac{NA}{n_i} \sqrt{s_x^2 + s_y^2}$.

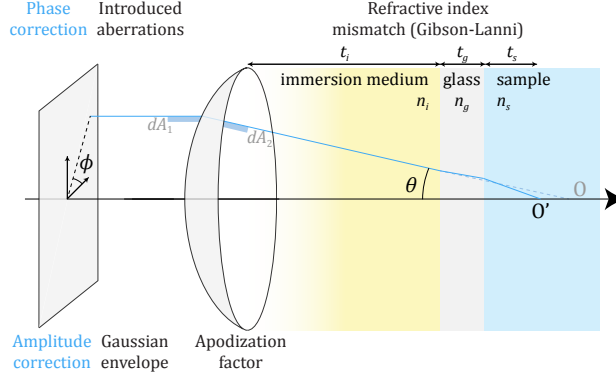


Figure 2: Correction factors and associated physical effects. Top: phase correction factors, either introduced on the incident field or due to refraction at different planes. Bottom: amplitude correction factors, to model an incident envelope or apodization factor for energy conservation.

where n_s, n_i, n_g are the refractive indices of the sample, immersion medium, and glass respectively, t_s, t_i, t_g are the thicknesses of the sample, immersion medium, and glass respectively, and their counterparts with stars are the design conditions.

A particular case proposed in [19] is commonly encountered: it is difficult in practice to assess the thickness of the immersion medium. Since this distance is manually tuned to obtain an optimal focus of a point emitter at depth t_s on the camera, this focusing condition gives the following relation:

$$t_i = t_s + n_i \left(-\frac{t_s}{n_s} - \frac{t_g}{n_g} + \frac{t_g^*}{n_g^*} + \frac{t_i^*}{n_i^*} \right) \quad (17)$$

which can be inserted in Eq. 16. This particular expression has first been derived for the spherical scalar case in [19] and extended to the spherical vectorial case in [40, 36].

3.4.2 Arbitrary Phase Aberrations

More general aberration models can be introduced to describe imperfections in the optical system for PSF engineering or wavefront shaping. They can be introduced experimentally via a phase mask or a spatial light modulator at the pupil plane. These aberrations are often parametrized by Zernike polynomials (a set of orthonormal polynomials defined on the pupil disk) or a direct fixed phase mask to obtain desired PSFs. We write it in the most general case:

$$W(\mathbf{s}) = \sum_{k=0}^{K-1} c_k Z_k(\mathbf{s}) + W_0(\mathbf{s}). \quad (18)$$

Eq. (18) is composed of an inner product of the first K Zernike polynomials and their corresponding coefficients c_k and an additional term W_0 which can be used to include special cases not covered by the Zernike polynomials, e.g. a vortex phase ramp that leads to a donut PSF, typically used in stimulated emission depletion microscopy.

Note that arbitrary phase aberrations described in Eq. (18) may not necessarily be axisymmetric, hence, they can only be applied to the most general, Cartesian parametrization.

3.4.3 Apodization Factor

The apodization factor is an amplitude correction factor to ensure energy conservation during the change of basis from cylindrical coordinates (incident field \mathbf{e}_{inc}) to spherical coordinates (far field \mathbf{e}_{∞}), which matters especially for high-NA objectives. Since areas of cross-sections are modified, the field is also rescaled accordingly. Such rescaling ensures that the differential areas dA_1 on the plane and dA_2 on the sphere, as shown in Fig. 2, remain consistent under the change of coordinates. The corresponding correcting factor is

$$A(\mathbf{s}) = \sqrt{\cos \theta} \quad (19)$$

when going from cylindrical to spherical in the focusing configuration of Fig. 1.

3.4.4 Gaussian Envelope

The incident illumination can also depart from a perfect uniform plane wave. In particular, we often assume a Gaussian envelope which can be expressed as

$$A(\mathbf{s}) = \exp \left\{ -\frac{\sin^2 \theta}{s_{\text{env}}^2} \right\} \quad (20)$$

where the constant s_{env} determines the size of the envelope.

4 Implementation

4.1 Design and Usage

We provide a high-performance open-source PyTorch library `psf-generator`⁵ to generate 2D and 3D PSFs. The library implements the four PSF models described in Section 3:

- `ScalarCartesianPropagator`,
- `ScalarSphericalPropagator`,
- `VectorialCartesianPropagator`, and
- `VectorialSphericalPropagator`.

In our unifying framework, these models encompass all previously proposed PSF models. Vectorial models are recommended for precise computations in high-NA scenarios. The Cartesian and spherical propagators perform equivalent integral computations, resulting in the same PSF. Both are proposed in our library as they differ in terms of computational efficiency and applicability. The spherical propagators are based on the axisymmetric assumption as described in Section 3.2. This includes all correction factors but the arbitrary phase aberrations introduced in Subsection 3.4.2.

Users can choose between various propagator types, configure physical parameters (e.g., numerical aperture, wavelength, and field of view), numerical parameters (e.g., image dimensions and number of z-planes). Our library also allows the users to freely apply any kind of correction factors tailored for their microscope on any chosen propagator. The propagators use these parameters to first define the far field (pupil) and propagate it to obtain the focus field (PSF). Finally, the user can visualize, save and export the generated PSF using our built-in utility functions. Written in PyTorch, the library easily integrates into deep learning workflows, leveraging PyTorch’s native features such as automatic differentiation. We use the ZernikePy library⁶ to generate Zernike polynomials.

4.2 Code Optimization

We have designed our library to follow the convention of PyTorch to benefit from its performance optimization to load data and parallelize computation. Namely, any tensor corresponding to a field has a shape of the form $(z, \text{channel}, x, y)$, which corresponds to the typical PyTorch convention $(\text{batch}, \text{channel}, x, y)$. Here, x and y correspond to the transverse sizes of 2D images. As computations are typically performed plane by plane, the `batch` dimension corresponds to the z axis. This enables efficient parallelization of Fourier transform for Cartesian models and numerical integration for spherical models. Finally, akin to grayscale versus RGB images, the `channel` dimension is equal to 1 for scalar models and 3 in the vectorial case.

The Cartesian parametrization relies on multiple calls of 2D Fourier transforms with efficient sampling to obtain the desired field of view and pixel size. Padding zeros and using the Fast Fourier Transform (FFT) directly would be inefficient and significantly increase computational costs, as the physical sizes of pixels are typically very small in localization microscopy. We have implemented a custom variant of the 2D FFT in PyTorch, enabling arbitrary pixel size without additional computational cost. It is based on the chirp Z-transform which can be equivalently written as a convolution and computed using three FFTs. The computational complexity of a single plane is still $O(n \log(n))$ with n the size of the transverse plane. The size of the Fourier transform is doubled as we only keep the valid convolution range. This method has been introduced in previous studies of the Cartesian models [16, 3, 29]. This approach also eliminates any artifacts caused by periodic boundary conditions, which are common with FFTs [3].

On the other hand, the spherical parametrization relies on fast and accurate evaluation of multiple one-dimensional integrals that involve the Bessel function of first order J_0 over the interval $[0, \theta_{\text{max}}]$ for a range of angles θ defined in Eq.

⁵https://github.com/Biomedical-Imaging-Group/psf_generator

⁶<https://pypi.org/project/ZernikePy/>

(5) for the scalar case. To maximize speed, we vectorize the computation of the batch of 1D integrals at different defocus distances via `torch.vmap`. Then, for each 1D integral, we adopt the composite Simpson’s rule [43] to benefit from its high accuracy, good numerical stability and minimal computational overhead. This is not applicable to the Cartesian case because the disk-shaped support of the pupil function introduces a discontinuity, which prevents the application of numerical integration acceleration. More details and a comparison with other methods will be presented in Figure 6 and Section 5.2.2. The computational complexity in this case is merely $O(n)$ with n the number of integration steps in the interval $[0, \theta_{\max}]$. Additionally, note that automatic differentiation of the Bessel functions is not natively supported by PyTorch as of version 2.3, so we also provide a differentiable version of the Bessel functions in our library as it is essential to learning-based tasks.

5 Results

5.1 PSF Gallery

We provide a gallery of PSFs to showcase different outputs of our library in Figure 3 and Figure 4. We use a wavelength of 632 nm, circular polarization for the vectorial models, and display the amplitude (in arbitrary units) of the beams for better contrast. Different 2D slices of the same 3D beam share the same dynamic range. We first compare the 3D unaberrated beams computed by the scalar and vectorial propagators for low- and high-NA. Two representative slices, one $x - y$ plane at the focus, the other $z - y$ plane through the center of the PSF, and vertical line profiles through the FOV center are shown in Figure 3. In the low-NA case, the resulting PSFs from both propagators are similar. The beams differ more from each other, as expected, in the high-NA case: the rings are blurred out as the energy is spread into different components of the focus field.

In Figure 4, we present other PSFs, computed using the vectorial propagator in the high-NA setting. The impact of the Gibson-Lanni correction factor on a beam is shown in Figure 4 (a)-(c). The values of the refractive indices and thicknesses of the sample, immersion medium and glass coverslip (c.f. Eq. (16)) are: $n_s = 1.3$, $n_i = 1.5$, $n_g = 1.5$, $t_s = 1 \mu\text{m}$, $t_g = 170 \mu\text{m}$, and t_i is computed using Eq. (17). We observe that the spherical aberration it introduces degrades the quality of the focus. We also show the donut PSF, which has a vortex phase mask in the pupil plane, (Figure 4 (d)-(f)) and the half-moon PSF, which has a π -jump in its pupil phase (Figure 4 (g)-(i)). Finally, we demonstrate an example of arbitrary phase aberrations using the Zernike polynomials in Figure 4 (j)-(l). Here, some amount of astigmatism is introduced, as is often done to encode defocus information [44], and we show the evolution of the beam shape along the z -axis.

5.2 Computational Performance

5.2.1 Speed Benchmark

We benchmark the runtime to compute a single 201×201 2D PSF image against the size of the pupil. The image is captured at focus and all input parameters take default values in our library. We compare the runtime of all four propagators on CPU and GPU and show the results in Fig. 5. The benchmarking was performed on a machine with an Intel i9-10900X CPU and an NVIDIA GeForce RTX 3090 GPU.

We observe that the runtime of all propagators increases with the size of the pupil on CPU. The Cartesian propagators (red) are faster than the spherical ones (blue) on smaller sizes (< 512 pixels) but slower on large sizes. This illustrates the difference in computational complexity of the different methods. Scalar propagators (dotted) are faster than their vectorial counterparts (solid), by roughly 1.5 times for Cartesian and 3 times for spherical cases. On GPU, Cartesian propagators are faster than on CPU at the same grid size and the curves (red) behave similarly; spherical propagators, however, exhibit a flat curve (blue) which indicates that they efficiently benefit from the GPU parallelization. The speed improvement between scalar and vectorial propagators is small, especially for the Cartesian case. Hence, vectorial propagators should be preferred over the scalar ones as the accuracy gain does not come at a high computational cost. Moreover, Cartesian propagators are recommended if one works with images of small sizes for both scalar and vectorial cases; while spherical propagators should be preferred for large sizes, especially when GPU is available.

5.2.2 Accuracy Benchmark

We benchmark the accuracy of both Cartesian and spherical scalar propagators with the analytic Airy disk for asymptotic limit (the Fourier transform of a perfect circular aperture):

$$F_{\text{AD}}(\rho) = \frac{2J_1(\rho)}{\rho}, \quad (21)$$

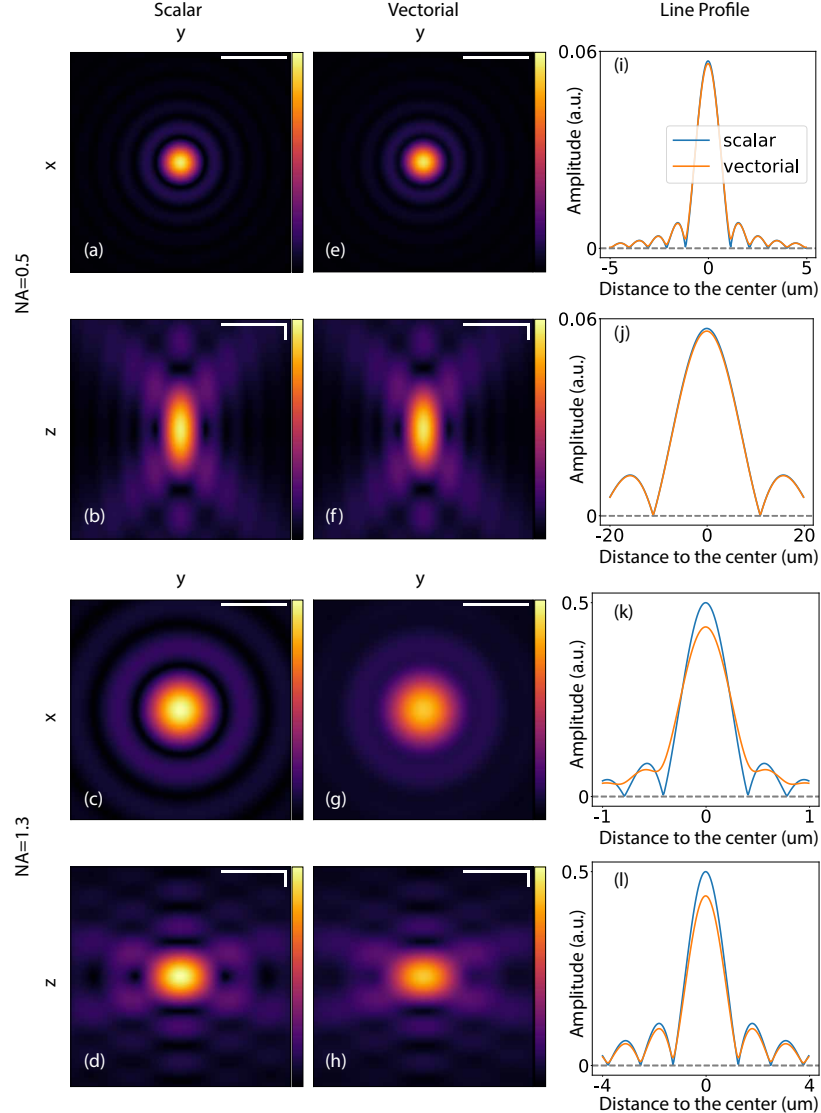


Figure 3: Comparison of an unaberrated PSF generated by the scalar ((a)-(d)) and vectorial with circular polarization ((e)-(h)) Cartesian propagators in the case of low-NA (0.5) (first two rows) and high-NA (1.3) (last two rows). (a), (e), (c), and (g): a slice of the $x - y$ plane. (b), (f), (d), and (h): a slice of the $z - y$ plane. (i)-(l): comparison of intensity profiles along a vertical line through the center of the PSFs. The x -axis represents the relative distance to the center of the image in micrometers. Scale bars represent $3 \mu\text{m}$ and $0.6 \mu\text{m}$ in the low- and high- NA cases, respectively. For images of $z - y$ planes ((b), (f), (d), and (h)), scale bars for the y and z axis are indicated by the horizontal and vertical bars, respectively.

where J_1 is the Bessel function of the first order of the first kind. As the Airy disk is the Fourier transform of a perfect unit modulus circular aperture, an additional factor $s_z = \cos \theta$ is introduced in Eqs. (3) and (5). This corresponds to a paraxial approximation.

The spherical integral is computed using two numerical integration rules: the Riemann rule (a first-order method) and the Simpson's rule (a fourth-order method). The error is the L_2 -norm of the difference between the output electric field E of the propagator and F_{AD}

$$\delta = \|E - F_{\text{AD}}\|_2. \quad (22)$$

We observe in Figure 6 that the error decreases as the number of points in the integration domain increases in all cases. The spherical propagator has a linear convergence rate using the Riemann rule (green) and 4th-order convergence rate

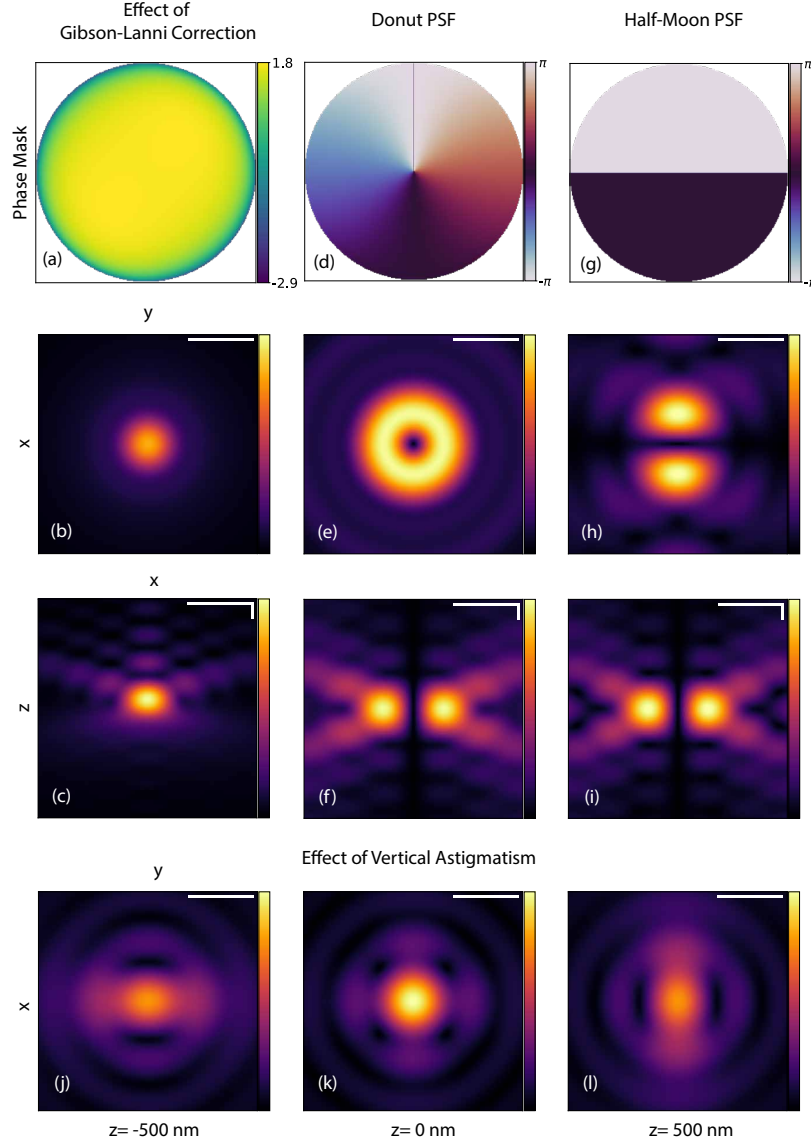


Figure 4: Examples of PSFs with different phase aberrations generated by the vectorial Cartesian propagator with high NA (1.3). ((a), (d), and (g)): Introduced phase masks at the pupil plane. ((b), (e), and (h)): Slice of the $x - y$ plane at $z = 0$. ((c), (f), and (i)): Slice of the $z - x$ plane at $y = 0$. ((j)-(l)): PSF with vertical astigmatism at three z -planes: at focus (k), 500 nm above (j), and below (l) focus. All PSFs generated with circular polarization, except the Half-Moon PSF where x -axis linear polarization is being used. The scale bars in all images represent $0.6 \mu\text{m}$.

using Simpsons' rule (blue), which correlates well with their expected accuracy. The Cartesian propagator, which is based on our custom FFT, shows a convergence rate between first- and second-order.

6 Conclusion

In this work, we have introduced a unifying theory for accurate PSF models, revisiting previous approaches and generalizing correction factors. This framework demonstrates the equivalence of Cartesian and spherical methods as different parametrizations of the same propagation integral, providing a simplified understanding of light propagation in high-NA systems.

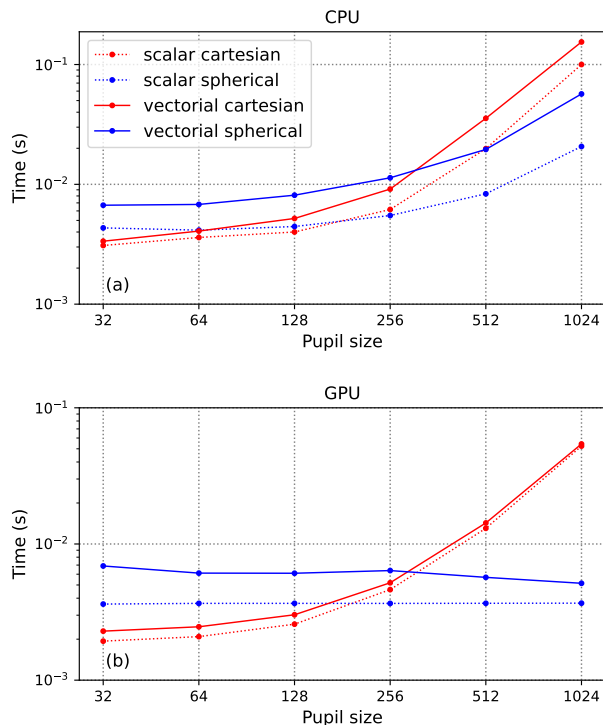


Figure 5: Speed benchmark. Time to generate a 201×201 PSF for different numerical sizes of the pupil, for the different four propagators, on CPU (a) and GPU (b). Each data point in the plots is averaged over 10 runs.

We have also developed a high-performance implementation in PyTorch, which is open-source and supported by comprehensive documentation. This library allows for efficient CPU/GPU computation of PSFs, with functionalities such as automatic differentiation that make it particularly suitable for optimization pipelines.

In practice, the choice of propagators depends on the symmetry of the pupil function. Based on our benchmark, for axisymmetric pupil functions, spherical propagators are recommended thanks to their high accuracy and scalability. They are also particularly amenable to GPU parallelization. For non-axisymmetric cases, such as those involving Zernike aberrations or specialized phase masks, Cartesian propagators are required. In all these cases, the difference in computational time is relatively modest for pupil sizes up to a few hundreds. Hence, the vectorial Cartesian propagator could be a solid default choice in most applications.

We hope for our Pytorch library to contribute to the rapidly growing field of applying deep neural networks on physical imaging models [45]. Learning-based methods have demonstrated their effectiveness in various applications, such as deconvolution [46, 47, 48] and 3D SMLM [49], with state-of-the-art deep-learning tools such as DeepSTORM [50] and DECODE [51]. For instance, some use cases of our framework include generating large reference datasets to train networks or adapting images based on physical rules to enable learning in self-supervised inversions [52] and generative adversarial networks [53].

Funding

Vasiliki Stergiopoulou acknowledges funding from the Swiss National Science Foundation under Grant CRSII5_213521, "DigiLight - Programmable Third-Harmonic Generation (THG) Microscopy Applied to Advanced Manufacturing". Jonathan Dong acknowledges funding from the Swiss National Science Foundation (Grant PZ00P2_216211).

References

- [1] C. Matthews and F. P. Cordelieres, "Metroloj: an imagej plugin to help monitor microscopes' health," in *ImageJ User & Developer Conference proceedings*, pp. 1–6, 2010.

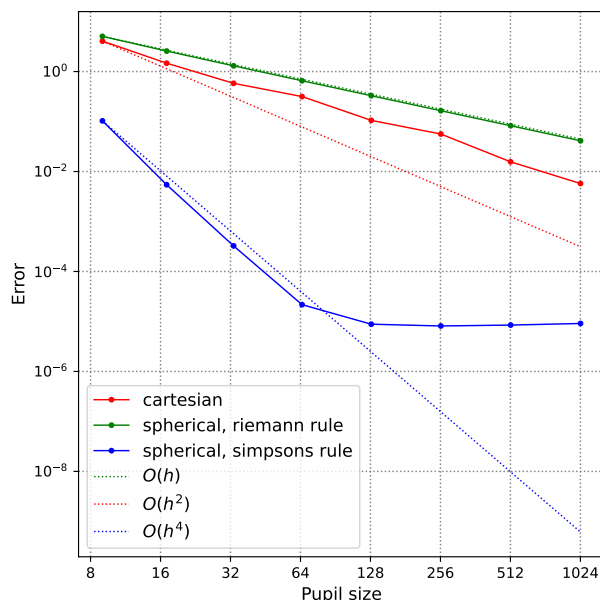


Figure 6: Accuracy benchmark of the Cartesian propagator (red) and the spherical propagator using the Riemann rule (green) and Simpsons' rule (blue). h is the step size of integration.

- [2] P. Theer, C. Mongis, and M. Knop, "Psfj: know your fluorescence microscope," *Nature methods*, vol. 11, no. 10, pp. 981–982, 2014.
- [3] R. H. D. Miora, E. Rohwer, M. Kielhorn, C. Sheppard, G. Bosman, and R. Heintzmann, "Calculating point spread functions: methods, pitfalls, and solutions," *Optics Express*, vol. 32, no. 16, pp. 27278–27302, 2024.
- [4] G. Nelson, I. Alexopoulos, M. Azevedo, F. Barachati, Y. Belyaev, M. T. Carvalho, Y. Cesbron, A. Dauphin, A. D. Corbett, L. Gelman, *et al.*, "Monitoring the point spread function for quality control of confocal microscopes," 2022.
- [5] M. Lelek, M. T. Gyparaki, G. Beliu, F. Schueder, J. Griffié, S. Manley, R. Jungmann, M. Sauer, M. Lakadamyali, and C. Zimmer, "Single-molecule localization microscopy," *Nature reviews methods primers*, vol. 1, no. 1, p. 39, 2021.
- [6] J.-B. Sibarita, "Deconvolution microscopy," *Microscopy Techniques*, pp. 201–243, 2005.
- [7] D. Sage, L. Donati, F. Soulez, D. Fortun, G. Schmit, A. Seitz, R. Quiet, C. Vonesch, and M. Unser, "Deconvolutionlab2: An open-source software for deconvolution microscopy," *Methods*, vol. 115, pp. 28–41, 2017.
- [8] R. Heintzmann and C. G. Cremer, "Laterally modulated excitation microscopy: improvement of resolution by using a diffraction grating," in *Optical biopsies and microscopic techniques III*, vol. 3568, pp. 185–196, SPIE, 1999.
- [9] M. G. Gustafsson, "Surpassing the lateral resolution limit by a factor of two using structured illumination microscopy," *Journal of microscopy*, vol. 198, no. 2, pp. 82–87, 2000.
- [10] T. Dertinger, R. Colyer, G. Iyer, S. Weiss, and J. Enderlein, "Fast, background-free, 3d super-resolution optical fluctuation imaging (sofi)," *Proceedings of the National Academy of Sciences*, vol. 106, no. 52, pp. 22287–22292, 2009.
- [11] V. Stergiopoulou, L. Calatroni, H. de Moraes Goulart, S. Schaub, and L. Blanc-Féraud, "COLORME: Super-resolution microscopy based on sparse blinking/fluctuating fluorophore localization and intensity estimation," *Biological Imaging*, vol. 2, 2022.
- [12] S. W. Hell, "Far-field optical nanoscopy," *science*, vol. 316, no. 5828, pp. 1153–1158, 2007.
- [13] F. Balzarotti, Y. Eilers, K. C. Gwosch, A. H. Gynnå, V. Westphal, F. D. Stefani, J. Elf, and S. W. Hell, "Nanometer resolution imaging and tracking of fluorescent molecules with minimal photon fluxes," *Science*, vol. 355, no. 6325, pp. 606–612, 2017.

- [14] Z. Marin, M. Graff, A. E. Barentine, C. Soeller, K. K. H. Chung, L. A. Fuentes, and D. Baddeley, “Pymevisualize: an open-source tool for exploring 3d super-resolution data,” *Nature methods*, vol. 18, no. 6, pp. 582–584, 2021.
- [15] B. Richards and E. Wolf, “Electromagnetic diffraction in optical systems, ii. structure of the image field in an aplanatic system,” *Proceedings of the Royal Society of London. Series A. Mathematical and Physical Sciences*, vol. 253, no. 1274, pp. 358–379, 1959.
- [16] M. Leutenegger, R. Rao, R. A. Leitgeb, and T. Lasser, “Fast focus field calculations,” *Optics express*, vol. 14, no. 23, pp. 11277–11291, 2006.
- [17] F. Aguet, “Super-resolution fluorescence microscopy based on physical models,” tech. rep., EPFL, 2009.
- [18] L. Novotny and B. Hecht, *Principles of Nano-Optics*. Cambridge: Cambridge University Press, 2 ed., 2012.
- [19] S. F. Gibson and F. Lanni, “Experimental test of an analytical model of aberration in an oil-immersion objective lens used in three-dimensional light microscopy,” *JOSA A*, vol. 8, no. 10, pp. 1601–1613, 1991.
- [20] H. Kirshner, A. François, D. Sage, and M. Unser, “3-d psf fitting for fluorescence microscopy: implementation and localization application,” *Journal of microscopy*, vol. 249, no. 1, pp. 13–25, 2013.
- [21] M. J. Nasse and J. C. Woehl, “Realistic modeling of the illumination point spread function in confocal scanning optical microscopy,” *Josa a*, vol. 27, no. 2, pp. 295–302, 2010.
- [22] M. C. Schneider, F. Hinterer, A. Jesacher, and G. J. Schütz, “Interactive simulation and visualization of point spread functions in single molecule imaging,” *Optics Communications*, vol. 560, p. 130463, 2024.
- [23] F. Caprile, L. A. Masullo, and F. D. Stefani, “Pyfocus—a python package for vectorial calculations of focused optical fields under realistic conditions. application to toroidal foci,” *Computer Physics Communications*, vol. 275, p. 108315, 2022.
- [24] S. Prigent, H.-N. Nguyen, L. Leconte, C. A. Valades-Cruz, B. Hajj, J. Salamero, and C. Kervrann, “Spitfir (e): a supermaneuverable algorithm for fast denoising and deconvolution of 3d fluorescence microscopy images and videos,” *Scientific Reports*, vol. 13, no. 1, p. 1489, 2023.
- [25] Y. Li, M. Mund, P. Hoess, J. Deschamps, U. Matti, B. Nijmeijer, V. J. Sabinina, J. Ellenberg, I. Schoen, and J. Ries, “Real-time 3d single-molecule localization using experimental point spread functions,” *Nature methods*, vol. 15, no. 5, pp. 367–369, 2018.
- [26] J. Dong, D. Maestre, C. Conrad-Billroth, and T. Juffmann, “Fundamental bounds on the precision of iscat, cobri and dark-field microscopy for 3d localization and mass photometry,” *Journal of Physics D: Applied Physics*, vol. 54, no. 39, p. 394002, 2021.
- [27] Y. Shechtman, S. J. Sahl, A. S. Backer, and W. E. Moerner, “Optimal point spread function design for 3d imaging,” *Physical review letters*, vol. 113, no. 13, p. 133902, 2014.
- [28] N. Opatovski, E. Nehme, N. Zoref, I. Barzilai, R. Orange Kedem, B. Ferdman, P. Keselman, O. Alalouf, and Y. Shechtman, “Depth-enhanced high-throughput microscopy by compact psf engineering,” *Nature Communications*, vol. 15, no. 1, p. 4861, 2024.
- [29] Y. Liu, J. Dong, J. A. Maya, F. Balzarotti, and M. Unser, “Point-spread-function engineering in minflux: optimality of donut and half-moon excitation patterns,” *Opt. Lett.*, vol. 50, pp. 37–40, Jan 2025.
- [30] J. Sinkó, R. Kákonyi, E. Rees, D. Metcalf, A. E. Knight, C. F. Kaminski, G. Szabó, and M. Erdélyi, “Teststorm: Simulator for optimizing sample labeling and image acquisition in localization based super-resolution microscopy,” *Biomedical optics express*, vol. 5, no. 3, pp. 778–787, 2014.
- [31] D. Sage, H. Kirshner, T. Pengo, N. Stuurman, J. Min, S. Manley, and M. Unser, “Quantitative evaluation of software packages for single-molecule localization microscopy,” *Nature methods*, vol. 12, no. 8, pp. 717–724, 2015.
- [32] S. Wieser and G. J. Schütz, “Tracking single molecules in the live cell plasma membrane—do’s and don’t’s,” *Methods*, vol. 46, no. 2, pp. 131–140, 2008.
- [33] H. Shen, L. J. Tauzin, R. Baiyasi, W. Wang, N. Moringo, B. Shuang, and C. F. Landes, “Single particle tracking: from theory to biophysical applications,” *Chemical reviews*, vol. 117, no. 11, pp. 7331–7376, 2017.
- [34] J. Griffié, T. Pham, C. Sieben, R. Lang, V. Cevher, S. Holden, M. Unser, S. Manley, and D. Sage, “Virtual-smlm, a virtual environment for real-time interactive smlm acquisition,” *bioRxiv*, pp. 2020–03, 2020.
- [35] D. Bourgeois, “Single molecule imaging simulations with advanced fluorophore photophysics,” *Communications Biology*, vol. 6, no. 1, p. 53, 2023.
- [36] P. Török and P. Varga, “Electromagnetic diffraction of light focused through a stratified medium,” *Applied optics*, vol. 36, no. 11, pp. 2305–2312, 1997.

- [37] P. J. W. Debye, *Der lichtdruck auf kugeln von beliebigem material*. PhD thesis, Ludwig-Maximilians Universität München, 1908.
- [38] E. Wolf and Y. Li, “Conditions for the validity of the debye integral representation of focused fields,” *Optics Communications*, vol. 39, no. 4, pp. 205–210, 1981.
- [39] A. Egner and S. Hell, “Equivalence of the Huygens–Fresnel and Debye approach for the calculation of high aperture point-spread functions in the presence of refractive index mismatch,” *Journal of Microscopy*, vol. 193, no. 3, pp. 244–249, 1999.
- [40] P. Török, P. Varga, Z. Laczik, and G. Booker, “Electromagnetic diffraction of light focused through a planar interface between materials of mismatched refractive indices: an integral representation,” *JOSA A*, vol. 12, no. 2, pp. 325–332, 1995.
- [41] J. Goodman, *Introduction to Fourier Optics*. McGraw-Hill physical and quantum electronics series, W. H. Freeman, 2005.
- [42] S. Liu, J. Chen, J. Hellgoth, L.-R. Müller, B. Ferdman, C. Karras, D. Xiao, K. A. Lidke, R. Heintzmann, Y. Shechtman, *et al.*, “Universal inverse modeling of point spread functions for smlm localization and microscope characterization,” *Nature Methods*, pp. 1–12, 2024.
- [43] J. Stoer and R. Bulirsch, *Introduction to Numerical Analysis*, vol. 12 of *Texts in Applied Mathematics*. New York, NY: Springer New York, 2002.
- [44] H. P. Kao and A. Verkman, “Tracking of single fluorescent particles in three dimensions: use of cylindrical optics to encode particle position,” *Biophysical Journal*, vol. 67, no. 3, pp. 1291–1300, 1994.
- [45] C. Belthangady and L. A. Royer, “Applications, promises, and pitfalls of deep learning for fluorescence image reconstruction,” *Nature methods*, vol. 16, no. 12, pp. 1215–1225, 2019.
- [46] M. Weigert, U. Schmidt, T. Boothe, A. Müller, A. Dibrov, A. Jain, B. Wilhelm, D. Schmidt, C. Broaddus, S. Culley, *et al.*, “Content-aware image restoration: pushing the limits of fluorescence microscopy,” *Nature methods*, vol. 15, no. 12, pp. 1090–1097, 2018.
- [47] Y. Li, Y. Su, M. Guo, X. Han, J. Liu, H. D. Vishwasrao, X. Li, R. Christensen, T. Sengupta, M. W. Moyle, *et al.*, “Incorporating the image formation process into deep learning improves network performance,” *Nature Methods*, vol. 19, no. 11, pp. 1427–1437, 2022.
- [48] K. Yanny, K. Monakhova, R. W. Shuai, and L. Waller, “Deep learning for fast spatially varying deconvolution,” *Optica*, vol. 9, no. 1, pp. 96–99, 2022.
- [49] D. Sage, T.-A. Pham, H. Babcock, T. Lukes, T. Pengo, J. Chao, R. Velmurugan, A. Herbert, A. Agrawal, S. Colabrese, *et al.*, “Super-resolution fight club: assessment of 2d and 3d single-molecule localization microscopy software,” *Nature methods*, vol. 16, no. 5, pp. 387–395, 2019.
- [50] E. Nehme, D. Freedman, R. Gordon, B. Ferdman, L. E. Weiss, O. Alalouf, T. Naor, R. Orange, T. Michaeli, and Y. Shechtman, “Deepstorm3d: dense 3d localization microscopy and psf design by deep learning,” *Nature methods*, vol. 17, no. 7, pp. 734–740, 2020.
- [51] A. Speiser, L.-R. Müller, P. Hoess, U. Matti, C. J. Obara, W. R. Legant, A. Kreshuk, J. H. Macke, J. Ries, and S. C. Turaga, “Deep learning enables fast and dense single-molecule localization with high accuracy,” *Nature methods*, vol. 18, no. 9, pp. 1082–1090, 2021.
- [52] H. Kobayashi, A. C. Solak, J. Batson, and L. A. Royer, “Image deconvolution via noise-tolerant self-supervised inversion,” *arXiv preprint arXiv:2006.06156*, 2020.
- [53] M. Cachia, V. Stergiopoulou, L. Calatroni, S. Schaub, and L. Blanc-Féraud, “Fluorescence image deconvolution microscopy via generative adversarial learning (fluogan),” *Inverse Problems*, vol. 39, no. 5, p. 054006, 2023.